UC Berkeley
UC Berkeley Previously Published Works

Title
Simulated Photoelectron Spectra of the Cyanide-Water Anion via Quasiclassical Molecular Dynamics

Permalink
https://escholarship.org/uc/item/6mx3k9h5

Journal
The Journal of Physical Chemistry A, 115(23)

ISSN
1089-5639

Authors
Lambrecht, Daniel S
Clark, Gary NI
Head-Gordon, Teresa
et al.

Publication Date
2011-06-16

DOI
10.1021/jp110334w

Peer reviewed

eScholarship.org Powered by the California Digital Library
University of California

Simulated photoelectron spectra of the cyanide-water anion via quasiclassical molecular dynamics

Daniel S. Lambrecht[1], Gary N. I. Clark[2,3] Teresa Head-Gordon[2,3], Martin Head-Gordon[1*]
[1]*Department of Chemistry, University of California, Berkeley*
[2]*Department of Bioengineering, University of California, Berkeley*
[3]*Physical Biosciences Division, Lawrence Berkeley National Laboratory*
Berkeley, California 94720 USA

We present the simulated photoelectron spectrum (PES) for cyanide-water $CN(H_2O)^-$ based on quasiclassical trajectory molecular dynamics (QCT-MD). Using density functional theory to generate trajectories and to calculate vertical detachment energies, we obtain simulated spectra that are in qualitative agreement with experiment. We obtain a theoretical 12 K→300 K temperature red shift of 0.1 eV as compared to an experimental redshift of 0.25 eV. The calculated linewidths of 0.3 eV are in excellent agreement with experiment. Our trajectories show that the temperature red shift as being dominated by dynamics within the basin of the N-bound minimum, however, at 300 K we predict conversion into the basin of the C-bound minimum, equilibrating at a 80:20 ratio of N- vs. C- bound mixture. We discuss the potential advantages of QCT-MD over anharmonic Franck-Condon analysis such as natural incorporation of anharmonicity (as necessary for weakly bound systems), and reduced computational scaling, but also drawbacks such as neglect of final-state (e.g. Duschinsky) effects.

*Corresponding author

INTRODUCTION

Photoelectron spectroscopy (PES) offers unique insight into the chemistry and physics of charged gas-phase species [1–4]. Thanks to the ability to mass select, PES is especially suited to study the size dependence of molecular properties within a homologous set of chemical systems. An application of particular interest is investigation of solvation effects in nanodroplets, in which droplets contain solvent molecules in different extremes of environment, ranging from surface molecules exposed to the vacuum to buried molecules experiencing a more bulk-like environment. These nanodroplets span the size regime between small clusters and the bulk, thus providing insight into the formation and ultimate stabilization of particular solvation structures.

Because of the increasing complexity of photoelectron spectra for large floppy clusters, it is very desirable to obtain simulated spectra in order to help interpret the experimental results. However, non-rigid molecules such as solvation clusters often exhibit large anharmonic effects [5], which are computationally costly to describe. Straightforward application of Franck-Condon analysis, the prevailing approach for PES simulation, exhibits an exponential scaling with the number of atoms if anharmonicity is fully included [6], and is thus only applicable to systems with only a few atoms (cf. Refs. [7,8]), although efficient new algorithms have been presented [9, 10]. Furthermore, dynamical effects may play an important role due to the flexible structure of the clusters, whereas Franck-Condon analysis is an inherently static method.

In this paper we propose the application of molecular dynamics simulations based on quasiclassical trajectories (QCT-MD) [11, 12] to the simulation of PES spectra [see references 13, 14 for reviews on the quasi-classical approximation]. While QCTs have been employed in the calculation of reactive scattering, vibrational spectra or quantum dots [11, 12, 15–17], to the best of our knowledge application of QCT-MD to PES calculation has not been presented before.

We illustrate the QCT-MD approach for simulating the photoelectron spectra of the cyanide-water anion, $CN(H_2O)^-$, a relatively simple system that contains interesting chemistry. As discovered by Wang et al. [15], the PES of $CN(H_2O)^-$ exhibits a remarkable red shift of 0.25 eV when going from 12 to 300 K. The red shift was explained qualitatively using arguments based on the vibrational wave functions for a simple two-basin model describing the conversion between two minima, $CN^-\text{---}H_1OH_2$ and $CN^-\text{---}H_2OH_1$ (cf. Fig. 5 of Ref. [18]). At low temperature the system resides in the (almost doubly degenerate) vibrational ground state, which has probability maxima at the equilibrium structure (4.54 eV detachment energy). At room temperature, the third and fourth excited states (v = 3, 4) are accessible, whose probability

densities have maxima at positions with significantly decreased detachment energies (4.38 eV and 4.49 eV, respectively), thus lending to the idea that this model can explain a red shift of up to 0.16 eV. Since it is claimed that vibrational effects are important in the explanation of the red shift, this is an ideal application for QCT-MD and subsequent analysis of trajectories to provide direct evidence for this proposed origin of peak positions and line widths of the photoelectron spectrum.

However, a more refined explanation needs to go beyond a single-mode model since cyanide-water has several anharmonic, coupled modes. Also, dynamical effects may play a role, e.g. because the barrier height for conversion between the N- and the C-bound isomers ($CN(H_2O)^-$ and $NC(H_2O)-$) is similar to that of the $CN-\text{---}H_1OH_2$ to $CN-\text{---}H_2O$ conversion. One also has to ask whether the Boltzmann weight of the vibrationally excited states v = 3, 4 would be big enough to explain the observed red shift. Finally, it is hard to compare individual detachment energies to a full experimental spectrum. Our aim is therefore to simulate the full photoelectron spectrum from QCT-MD and to use the comparison of the simulated and the experimental photoelectron spectra to validate the trajectories. After the validation step, we use the trajectories to extract information on the structure and dynamics of the system. In summary, we obtain a theoretical 12 K→300 K temperature red shift of 0.1 eV as compared to an experimental red shift of 0.25 eV, while the calculated linewidths of 0.3 eV are in excellent agreement with experiment. Our trajectories support a previous model [18] that explains the temperature red shift as being dominated by dynamics within the basin of the N-bound minimum. However, our calculations lead to a refined picture: At 300 K we predict conversion into the basin of the C-bound minimum, equilibrating at a 80:20 N- vs. C-bound mixture.

II. COMPUTATIONAL METHODS

A. Benchmarks of relative energies and vertical detachment energies

In order to obtain reliable quasi-classical trajectories and photoelectron spectra, we need a method that yields reliable geometries, relative energies and detachment energies of the cyanide-water system. As a compromise between computational speed and accuracy we chose the popular B3LYP density functional [19, 20] in combination with a 6-311++G** Pople basis [21]. We used a development version of the Q-Chem program package [27] to generate all results.

The stationary points of the cyanide-water system calculated at this level of theory are

shown in Fig. 1. We observe that the structures compare well with high-level quantum mechanical results [18], although the TS1 structure is slightly different: in our structure both hydrogen atoms are facing the cyanide, whereas the reported structure [18] has one dangling hydrogen. The 6-311++G** basis is probably the minimum basis required to describe the system properly, because using the smaller 6-31+G* basis set led to a spurious transition state structure that cannot be found in any of the high-level calculations. Fig. 2 compares the B3LYP/6-311++G** energies for the stationary points with high-level ab initio results up to the CCSD(T)/aug-cc-pVQZ level. The agreement between B3LYP/6-311++G** and the CCSD(T)/aug-cc-pVQZ reference energies is good except for a slight overestimation of the energy for TS1.

MP2 also performs well on the stationary points compared to CCSD(T) provided that a sufficiently large basis is used (cf. weak MP2/6-31+G* performance). However, the MP2 vertical detachment energies (VDEs) are in lesser agreement with the reference calculations, whereas B3LYP/6-311++G** yields a reasonable agreement of the VDEs with high-level coupled cluster results throughout (see Fig. 3(a)). Although B3LYP overestimates the CCSD(T) detachment energies of min1 and min2 by 0.23 and 0.19 eV, respectively, relative trends are reproduced satisfactorily (Fig. 3(b)). For example, the shift between the carbon- and the nitrogen-bound minima (min2 and min1) is reproduced to within 0.04 eV. Since the B3LYP errors are quite systematic, we shift all calculated spectra (described below) by -0.23 eV to obtain better comparability to experiment. The biggest B3LYP/6-311++G** error in relative detachment energies is observed for TS1 with up to 0.10 eV relative to the CCSD(T) level. We have recalculated the CCSD(T) energy at the B3LYP geometry and found that the agreement is much better (open black squares in Fig. 3(a) and 3(b)). This larger detachment energy of our B3LYP TS1 structure can be rationalized by recalling that two hydrogen atoms are facing the cyanide (as opposed to one dangling hydrogen), thus providing stronger stabilization of the excess electron.

We also tested other density functionals such as the long-range corrected ωB97X and long-range + dispersion corrected ωB97X-D density functionals [24, 25], but observed only minor improvements, thus we employed the slightly faster B3LYP functional. It is possible, however, that the long-range correction becomes more important for larger clusters due to stronger self-interaction errors. This will be tested carefully for our upcoming calculations on larger clusters. Additionally we tested the B3LYP performance in combination with other basis

sets including larger Pople-style and correlation consistent basis sets of up to aug-cc-pVTZ level. No significant advantages over the 6-311++G**basis was found. In fact, for very large basis sets a deterioration of the quality was found, which is a known defect of DFT for anionic systems [26]. Overall, the amounts by which the relative detachment energies vary between the different stationary points are smaller at the B3LYP level than for the CCSD(T) reference. It can therefore be expected that the B3LYP-simulated temperature shifts are smaller than the experimental or the CCSD(T) ones.

We used a simple sanity check to test whether the experimental linewidths can also be reproduced at the chosen level of density functional theory. The experimental half-widths for 12 K and 300 K are both on the order of 0.3 eV. While we expect that the red shift is mainly due to the solvation environment, the CN stretching mode should account for most of the linewidth, which would explain why essentially no broadening is observed when going from 12 K to 300 K. Indeed if we calculate the differences in detachment energies between the classical turning points of the CN stretch vibration, the min1 equilibrium structure and TS2, we can obtain a maximum linewidth on the order of 0.2 eV. While this is somewhat smaller than the experimental line width, it is encouraging to get such a reasonable estimate with such a crude model.

B. Molecular dynamics simulation of photodetachment spectra

In order to obtain a full comparison of theory and experiment on the cyanide-water anion, we performed quasiclassical molecular dynamics simulations to generate theoretical spectra at 12 K and 300 K. As discussed in the literature [18], vibrational effects may be very important in the sampling of the transition state regions and thus the observation of a red shift. We therefore employ the quasiclassical approximation, which puts vibrational energy into each normal mode when setting up the initial velocities (as opposed to a purely classical MD, which uses a thermal Boltzmann distribution for the initial kinetic energy). The initial conditions are chosen such that the occupation numbers of the vibrational states for each mode follow a Boltzmann distribution for quantum harmonic oscillators at the simulation temperature (see Appendix A for a detailed account). The rest of the trajectory is then governed by classical mechanics.

As shown in Figure 4, at least 500–1,000 trajectories are required to obtain a reasonably converged initial vibrational distribution. The fact that the cyanide-water system is still relatively small makes it feasible to generate reference trajectories using a first-principles approach. For the quantum chemical reference trajectories we use the B3LYP density functional with a 6-

311++G** basis set, which provides reasonable agreement with high-level *ab initio* approaches (see section II A). We use a time step of 0.48fs, which is short enough to give on the order of 20 snapshots per period of the fastest vibration (OH stretch, 3878 cm^{-1}, 8.8 fs). The maximum simulation time for each trajectory is 3 ps, which is long enough to capture approximately 10 periods for the slowest mode (81 cm^{-1}, 0.3 ps) and thus should be long enough to sample the most important motions of the system. The spectra are then generated by calculating histograms from the detachment energies calculated at the B3LYP/6-311++G** level of theory, sampling every fifth step (i.e. every 2.4 fs) along the MD trajectory. The sampling step size is chosen to avoid overly-correlated sampling but at the same time to give enough resolution for the fastest vibrations. The QCT method is part of a development version of the Q-Chem program package [15], and will be included in the upcoming Q-Chem 4.0 release.

C. Validity of the quasiclassical approximation

A problem in the application of the quasi-classical approximation is that when the system is being propagated classically, the quantum laws of energy quantization do not apply anymore. While in a full quantum calculation, energy exchange between modes can only occur when certain resonance conditions are met, or when the inter-mode coupling terms are big, the classical equations of motion allow for the transfer of arbitrary amounts of energy. That makes it much easier for kinetic energy to "spill" from one mode to another [28], typically from hard (high-energy) into soft (low-energy) modes. Unfortunately, the QCT breakdown becomes more pronounced as the number of modes increases, but correction schemes exist [28], but for the present application it appears safe to simply restrict the data sampling to a reduced time scale when the QCT is valid.

To define the time scale over which the QCT remains valid, we monitor the percentage of TS1 barrier crossing (i.e. min1→min2 conversion) as a function of simulation time [36]. To that end we extract geometries from the MD trajectories every 0.12 ps and perform a geometry optimization. If the geometry relaxes into the min1 structure, we count the structure to the min1 basin, and similarly for the min2 structures. The resulting basin populations are shown in Fig. 5 for an average over 1,000 trajectories at 300 K and 100 trajectories at 12 K. With a barrier height on the order of 3kcal/mol and a vibrational period of 0.1-0.3 ps, it can be estimated from transition state theory that at 300 K the percentage of min1→min2 conversions can be on the order of 7-20% within 3 ps. For 12 K we expect 0% crossing during the whole simulation time.

Comparing these numbers with Fig. 5, we observe that the 300 K results are within a reasonable range for the whole course of the simulation. The percentage population plot also reveals that it takes on the order of 1.4 ps for the 300 K population to equilibrate. The 12 K shows crossing rates of less than 2-3% for up to 2.1 ps, but after that the min1→min2 conversion is clearly too high, probably as a result of the breakdown of the quasiclassical approximation. We therefore conclude that data sampled in the time range from 1.4 ps to 2.1 ps is the valid regime of the quasiclassical approximation.

D. Weighting of spectral data from quasiclassical trajectories

For low temperatures, the classical trajectories differ significantly from the quantum distributions: while the square of the ground-state vibrational wave function is largest at zero displacement, the classical oscillator spends most of its time close to the classical turning points and the least time at the equilibrium distance. Classical and quasiclassical trajectories therefore over sample the classically preferred regions, whereas the region close to the equilibrium structure is under sampled. A very drastic example of the consequences is shown in Fig. 6. Without proper quantum weighting, the simulated photoelectron spectrum of CN^- splits into two peaks that correspond to distributions about the two classical turning points. The experimental spectrum shows only one peak (peak center shown as dotted grey line).

We have therefore weighted our spectral data such that data points corresponding to geometries with large vibrational probability receive stronger weights. This is achieved by multiplying the histogram intensities with a weight, *w*, that is calculated as the sum of the wavefunction squares for all minima at the corresponding geometry:

$$w = \sum_{Min} \Psi_{vib}^2 (Min) \tag{1}$$

For reasons of practicality, we use the harmonic vibrational wavefunctions for the weighting. Further details on the formalism can be found in Appendix B. The effect of the quantum weighting (wQCT) is shown for CN− in Fig. 6. The two peaks are transformed into essentially one peak centered about the experimental detachment energy. Although a small peak splitting remains, the agreement with experiment is much better.

For the CN(H2O)− system, we consider two basins, min1 and min2 with two isomers each (H_1 and H_2), and 9 vibrational modes. For illustration, we show the wave function squares for 12 K and 300 K for the four softest normal modes in Fig. 7. The system has five rather soft

intermolecular modes (81-887 cm^{-1}) that can be envisioned as frustrated translations and rotations and 4 internal, rather hard modes (1696-3877 cm^{-1}) that correspond to the water bend, CN stretch, and the symmetric and asymmetric OH stretch. As Fig. 7 shows, modes 1-4 clearly follow quantum distributions at 12 K. The corresponding classical distribution would be peaked at the classical turning points, ±1 in unitless displacement coordinates. At 300 K the distribution for the softest modes (1 and 2) is broadened considerably, but still rather resembles a quantum distribution (because the Boltzmann weight of the highly excited and thus "more classical" states is still quite small). However, the distribution is already closer to a classical distribution, i.e. the probability is spread out from the center to the corners. The distribution of the harder modes (5-9) remains essentially unchanged when going from 12 K to 300 K.

III. RESULTS

The simulated 12 K and 300 K cyanide-water spectra are shown in Fig. 8 for trajectories originating in min1 (Fig. 8a), and for trajectories starting within min2 (Fig. 8b). For comparison we have also included the simulated CN− spectrum. Vertical dotted lines indicate the experimental VDEs for CN− at 3.86 eV and for min1 (CN(H2O)−) at 4.54 eV. At 4.63 eV we have marked the CCSD(T) VDE for min2 (NC(H2O)−). All simulated spectra are quantum-weighted as described above. We note, however, that the unweighted and weighted 300 K spectra are essentially identical. This is an important result, as it suggests that unweighted QCT-MD results can be used for high-temperature spectra, which enables a full anharmonic treatment at high temperstures (as opposed to harmonic quantum weights as currently employed). The overall agreement of the simulated min1 spectrum with the experimental spectrum is very good. We can reproduce a $CN^- \rightarrow CN(H2O)^-$ solvation shift of 0.7 eV as compared to an experimental value of 0.68 eV. The temperature red shift is qualitatively correct, although with a value of 0.1 eV it is smaller than the experimentally observed shift of 0.25 eV. However, this was already anticipated from the benchmark calculations, since B3LYP underestimated all relative shifts (see section IIA). Finally, the simulated peak widths at half maximum of 0.3 eV are in excellent agreement with experiment. We remark that purely classical MD simulations at 300 K yielded line widths of less than 0.1 eV, while the peaks from 12 K classical MD had essentially zero width.

The spectra from trajectories starting in min2 (Fig. 8(b)) show less good agreement with experiment. This supports earlier claims [18] that the photoelectron spectrum is mainly

determined by min1. However, with a min1→min2 conversion rate of 20% (see Fig. 5), our simulations suggest that the explanation that the system remains in the basin of min1 and that only TS2 gives rise to the red shift probably [18] has to be refined. The system does not remain solely in the basin of min1, and TS2 is not the only transition state that is sampled. Rather, our trajectories suggest that TS1 (converting min1 into min2 and vice versa) is also sampled to a certain extent. It is interesting to see that, although the detachment energies for min2 are blue-shifted rather than red shifted, the min1 spectrum still shows an overall temperature red shift. The observed overall red shift probably results from a superposition of a red shift associated with TS2 (and possibly TS1) sampling, and a smaller blue shift due to crossing into the min2 basin.

Although the agreement with experiment is not yet fully satisfactory, the quality of the results is certainly surprising, given that a number of approximations had to be made in order to make the calculations feasible. The level of theory employed to calculate the detachment energies (B3LYP/6-311++G**) probably causes the biggest fraction of the remaining error, since the relative shifts are generally underestimated. Furthermore, the quasiclassical approximation can introduce kinetic energy spilling from high- to low-energy modes, thus leading to spurious TS1 crossing, which reduces the observed red shift. At least for the low-energy spectra it would be desirable to include more quantum behavior in the trajectories, for example via centroid or ring polymer molecular dynamics (see [29] for an application in infrared spectroscopy). Also it would be desirable to go beyond the harmonic approximation for the low-temperature quantum weights. However, the fact that the effect of quantum weighting is negligible for the 300 K spectra makes us optimistic for future applications to investigate solvation shifts (rather than temperature shifts). Another restriction was the total number of trajectories that we were able to run within a reasonable amount of time (on the order of 1,000 trajectories per minimum). One would have to sample more trajectories to guarantee a better convergence of the vibrational distribution and phases. However, we did not observe qualitative changes when increasing the number of trajectories from a few 100's to 1,000. In summary, we have demonstrated the feasibility of calculating photoelectron spectra and have demonstrated that it yields qualitatively correct results.

IV. DISCUSSION AND CONCLUSIONS

Using a quasiclassical molecular dynamics approach, we have calculated the theoretical photoelectron spectra for $CN(H2O)^-$ at 12 K and 300 K. Our approach yields qualitative

agreement to the experimental spectra: the calculated redshift for going from 12 K to 300 K is 0.1 eV compared to an experimental shift of 0.25 eV [18], while the calculated peak widths of 0.3 eV are in excellent agreement with the experimental widths. Although the agreement with experiment is not yet fully satisfactory, the quality of the results is certainly surprising, given that a number of approximations had to be employed in order to make the calculations feasible. First, the quasiclassical approach is only an approximation to the full quantum dynamics and final-state effects are neglected. Second, we used B3LYP to generate trajectories, which shows some deviations from high-level quantum potential energy surfaces. Third, while performing quite well for many geometries, the B3LYP VDEs show deviations from high-level results that are on the order of the experimental red shift. Finally, the total number of trajectories that we were able to run within a given amount of time was limited to on the order of 1,000.

The QCT-MD approach has a number of advantages over Franck-Condon analysis for applications to floppy systems. Due to the steep computational scaling of anharmonic Franck-Condon analysis, its applicability is limited to small systems comprising on the order of a few atoms [7]. In contrast, QCT-MD is tractable for any system size for which an MD simulation is possible, i.e. tens or even hundreds of atoms, and anharmonic effects are included naturally by propagating the system on the (untruncated) potential energy surface. QCT-MD is easy to implement using existing molecular dynamics code, exploiting all existing methodological and technical developments like linear-scaling methods (cf. [30] for a review) or parallelization [27]. In addition to spectral information, QCT-MD delivers all information that can be extracted from MD simulations, like population of different minima or transition states and thus offers intuitive insight into the underlying chemistry and physics. The price for the decreased computational scaling of QCT-MD is that the calculated intensities do not include final-state effects (e.g. the Duschinsky effect [7]). As a result, the QCT-MD spectra lack some features, but this is not a major limitation since the experimental photoelectron spectra for solvation clusters are often not very highly resolved. We thus believe that QCT-MD is an important step toward the PES simulation of larger clusters, along with other approaches [31].

To give the reader an impression of the computational cost to evaluate the PES of $CN(H2O)^-$, the trajectory calculations took 6 weeks on an average of 50-80 cores. Detachment energies for 100 trajectories can be calculated within 2–3 days on a computer cluster with 24 cores. However, it is also possible to generate the trajectories at a lower level of theory, e.g. using empirical force fields, and then to gather spectral information at a higher (quantum

chemical) level of theory only for a relatively small number of points along the trajectory. The cost of such a joint MM/QM calculation could be roughly an order of magnitude lower than determining the trajectory on the QM potential energy. We will present such a joint approach in an upcoming publications, where we investigate a range of aqueous clusters with the help of the polarizable force field AMOEBA [32-35].

ACKNOWLEDGMENTS

This work was supported by the National Science Foundation under grant no. CHE- 0535710. M.H.G. is a part-owner of Q-Chem Inc. We thank Dr. Sudip Chakrabarty for useful discussions.

REFERENCES

[1] Simons, J. Molecular Anions. J. Phys. Chem. A 2008, 112, 6401-6511.

[2] Neumark, D. J. Chem. Phys. Probing chemical dynamics with negative ions. 2006, 125, 132303-1--132303-15.

[3] Wang, X.; Sergeeva, A.; Yang, J.; Xing, X.; Boldyrev, A.; Wang, L. Photoelectron Spectroscopy of Cold Hydrated Sulfate Clusters, SO42−(H2O) n (n= 4− 7): Temperature-Dependent Isomer Populations. J. Phys. Chem. A 2009, 113, 5567-5576.

[4] Wang, X.; Wang, L. Photoelectron Spectroscopy of Multiply Charged Anions. Ann. Rev. Phys. Chem. 2009, 60, 105-126.

[5] Nesbitt, D. High-resolution infrared spectroscopy of weakly bound molecular complexes. Chem. Rev. 1988, 88, 843-870.

[6] Ervin, K.; Ramond, T.; Davico, G.; Schwartz, R.; Casey, S.; Lineberger, W. Naphthyl Radical: Negative Ion Photoelectron Spectroscopy, Franck− Condon Simulation, and Thermochemistry. J. Phys. Chem. A 2001, 105, 10822-10831.

[7] Wang, H.; Zhu, C.; Yu, J.-G.; Lin, S. H. Anharmonic Franck-Condon Simulation of the Absorption and Fluorescence Spectra for the Low-Lying S-1 and S-2 Excited States of Pyridine. J. Phys. Chem. A 2009, 113, 14407-14414.

[8] Wang, C.; Liu, C.; Liu, Y.; Liang, J.; Cui, Z. Calculation of Franck-Condon factors and simulation of photoelectron spectroscopy of D2CO: Including Duschinsky effects. J. Mol. Struc-Theochem 2010, 948, 25-30.

[9] Barone, V.; Anharmonic vibrational properties by a fully automated second-order perturbative approach. J. Chem. Phys. 2005, 122, 014108-1—014108-10.

[10] Santoro, F.; Improta, R.; Lami, A.; Bloino, J.; Barone, V. Effective method to compute Franck-Condon integrals for optical spectra of large molecules in solution. J. Chem. Phys. 2007, 126, 084509-1—084509-13.

[11] Karplus, M.; Porter, R.; Sharma, R. Exchange Reactions with Activation Energy. I. Simple Barrier Potential for (H, H). J. Chem. Phys. 1965, 43, 3259-3287.

[12] Porter, R.; Raff, L.; Miller, W. Quasiclassical selection of initial coordinates and momenta for a rotating Morse Oscillator. J. Chem. Phys. 1975, 63, 2214-2218.

[13] Porter, R. Molecular trajectory calculations. Ann. Rev. Phys. Chem. 1974, 25, 317-355.

[14] Sewell, T.; Thompson, D. Classical Trajectory Methods for Polyatomic Molecules. Int J Mod Phys B 1997, 11, 1067-1112.

[15] Rio, C. M. A.; Wang, W.; Brandao, J. Quasiclassical trajectory calculations of the H + O-2 and O + OH reactions on spectroscopically accurate modified DMBE IV PESs. J. Mol. Struc. - Theochem 2010, 946, 2-6.

[16] Gamallo, P.; Martinez, R.; Sayos, R.; Gonzalez, M. Quasiclassical dynamics and kinetics of the N+NO -> N-2+O, NO+N atmospheric reactions. J. Chem. Phys. 2010, 132, 144304-1—144304-9.

[17] Merkulov, I. A.; Alvarez, G.; Yakovlev, D. R.; Schulthess, T. C. Long-term dynamics of the electron-nuclear spin system of a semiconductor quantum dot. Phys. Rev. B 2010, 81, 115107-1—115107-13.

[18] Wang, X.; Werhahn, J.; Wang, L.; Wang, L.; Kowalski, K.; Lauberau, A.; Xantheas, S. J. Observation of a Remarkable Temperature Effect in the Hydrogen Bonding Structure and Dynamics of the CN−(H2O) Cluster. Phys. Chem. A 2010, 113, 9579-9584.

[19] Becke, A. Density-functional exchange-energy approximation with correct asymptotic behavior. Phys. Rev. A 1988, 38, 3098-3100; Becke, A. A new mixing of Hartree–Fock and local density-functional theories. J. Chem. Phys. 1993, 98, 1372-1378; Becke, A. Density-functional thermochemistry. IV. A new dynamical correlation functional and implications for exact-exchange mixing. J. Chem. Phys. 1996, 104, 1040-1045.

[20] Yang, W.; Parr, R.; Lee, C. Development of the Colle-Salvetti correlation-energy formula into a functional of the electron density. Phys. Rev. A 1986, 37, 785-789.

[21] Krishnan, R.; Binkley, J.; Seeger, R.; Pople, J. Self-consistent molecular orbital methods. XX. A basis set for correlated wave functions. J. Chem. Phys. 1980, 72, 650.

[22] Dunning, T. Gaussian basis sets for use in correlated molecular calculations. I. The atoms

boron through neon and hydrogen. J. Chem. Phys. 1989, 90, 1007-1024.

[23] Kendall, R.; Dunning, T.; Harrison, R. Electron affinities of the first-row atoms revisited. Systematic basis sets and wave functions. J. Chem. Phys. 1992, 96, 6796-6807.

[24] Chai, J.-D.; Head-Gordon, M. Systematic optimization of long-range corrected hybrid density functionals. J. Chem. Phys. 2008, 128, 084106-1—084106-15.

[25] Chai, J.-D. ; Head-Gordon, M. Optimal operators for Hartree-Fock exchange from long-range corrected hybrid density functionals. Chem. Phys. Lett. 2008, 467, 176-178.

[26] Jensen, F. Describing anions by density functional theory: Fractional electron affinity. J. Chem. Theor. Comp. (2010) 6, 2726-2735.

[27] Shao, Y.; Fusti Molnar, L.; Jung, Y.; Kussmann, J.; Ochsenfeld, C.; S. T. Brown, A. T.B. Gilbert, L. V. Slipchenko, S. V. Levchenko, D. P. ONeill, et al., Advances in methods and algorithms in a modern quantum chemistry program package. Phys. Chem. Chem. Phys. 2006, 8, 3172-3191.

[28] Czako, G.; Kaledin, A. L.; Bowman, J. M. A practical method to avoid zero-point leak in molecular dynamics calculations: Application to the water dimmer. J. Chem. Phys. 2010, 132, 164103-1—164103-6.

[29] Witt, A.; Ivanov, S.; Shiga, M.; Forbert, H.; Marx, D. On the applicability of centroid and ring polymer path integral molecular dynamics for vibrational spectroscopy. J. Chem. Phys. 2009, 130, 194510-1—194510-15.

[30] Ochsenfeld, C.; Kussmann, J.; Lambrecht, D. S. Linear-scaling methods in quantum chemistry. Rev. Comp. Chem. 2004, 23, 1-82.

[31] Wang, X.-B.; Kowalski, K.; Wang, L.-S.; Xantheas, S. S. Stepwise hydration of the cyanide anion: A temperature-controlled photoelectron spectroscopy and ab initio computational study of CN[sup −](H[sub 2]O)[sub n], n=2–5. J. Chem. Phys. 2010, 132, 124306-1—124306-10.

[32] Ponder, J. W.; Wu, C.; Ren, P.; Pande, V. S.; Chodera, J. D.; Schnieders, M. J.; Haque, I.; Mobley, D. L.; Lambrecht, D. S.; Distasio, R. A.; Head-Gordon, M.; Clark, G.N.; Johnson, M. E.; Head-Gordon, T. Current Status of the AMOEBA Polarizable Force Field. J. Phys. Chem. B 2010, 114, 2549-2564.

[33] Ren, P.; Ponder, J. Consistent treatment of inter- and intramolecular polarization in molecular mechanics calculations. J. Comput. Chem. 2002, 23, 1497-1506.

[34] Ren, P.; Ponder, J. Polarizable atomic multipole water model for molecular mechanics simulation. J. Phys. Chem. B 2003, 107, 5933-5947.

[35] Ponder, J.; Case, D. Force fields for protein simulations. Adv. Prot. Chem. 2003, 66, 27-86.

[36] We have also tested monitoring the kinetic energy within each normal mode as a function of simulation time, but encountered problem in the applicability to this system due to anharmonicity and large-amplitude motion.

APPENDIX A: INITIAL CONDITIONS FOR QUASICLASSICAL TRAJECTORY CALCULATIONS

We describe here in detail our procedure for initialization of quasiclassical trajectory calculations, hoping that this may be useful for others since we found the original literature [11, 12] to be very terse regarding the practical aspects. In our implementation the initial velocities are chosen according to the vibrational Boltzmann distribution. Other degrees of freedom, like rotations, are currently neglected.

1. Obtaining the initial distribution over vibrational states with temperature, θ

We use the harmonic approximation throughout. The vibrational energy for normal mode m in state ν is then

$$E_{vib}^{m}(\nu) = h\nu_m\left(\nu + \frac{1}{2}\right) \tag{A1}$$

and the modes are uncoupled such that the assignment can be performed for all modes independently. The probability p_ν^m that the mth mode is in state ν can be determined from the Boltzmann factor,

$$p_\nu^m = \frac{1}{Z_m}\mathrm{e}^{-\frac{E_{vib}^{m}(\nu)}{k\theta}} = \frac{1}{Z_m}\mathrm{e}^{-\frac{\Theta_m\left(\nu+\frac{1}{2}\right)}{\theta}} \tag{A2}$$

where Θ_m is the vibrational temperature of the mode and $Z_m = \sum_\nu \mathrm{e}^{-\frac{E_{vib}^{m}(\nu)}{k\theta}}$ is the vibrational partition function.

We generate a random number $p \in [0, 1]$ and find ν according to

$$\nu = -\left\lceil \frac{\theta \ln p_\nu^m}{\Theta_m} + \ln Z_m \right\rceil, \tag{A3}$$

where ⌈ ⌉ denotes the ceiling function. This assignment distributes the initial vibrational levels according to Boltzmann statistics at temperature θ.

2. Obtaining initial normal-mode velocities

For the classical harmonic oscillator the sum of the kinetic energy and potential energy V (qm) is equal to the total energy:

$$E_{vib}^{m}(v) = \frac{1}{2}\mu_m \dot{q}_m^2 + V\left(q_m\right) \tag{A4}$$

where μ_m is the reduced mass and q_m ($\dot{q}_m$) is the normal-mode displacement (velocity). From the initial geometry and the vibrational energy we can therefore calculate the initial velocity along mode m as

$$\dot{q}_m^{(0)} = \pm\sqrt{2\frac{E_{vib}^{m}(v) - V\left(q_m^{(0)}\right)}{\mu_m}}, \tag{A5}$$

Note that the initial geometries have to be confined to within the classical turning points in order to obtain real-valued velocities.

We choose the sign of the initial geometries at random and for the sake of simplicity start all trajectories from the equilibrium structure (i.e. V (q(0) m) = 0). In future studies we will test whether it is beneficial to sample initial geometries according to the vibrational probability distribution, e.g. with respect to shorter equilibration times.

3. Transformation to Cartesian coordinates

The normal-mode velocities $\dot{q}_m$ need to be transformed to Cartesian velocities $\dot{\mathbf{r}}_a = \left(\dot{x}_a, \dot{y}_a, \dot{z}_a\right)^T$ for each atom a. This is done using the matrix $\mathbf{U} = \left(U_{m,ai}\right)$ that diagonalizes the nuclear Hessian:

$$\mathbf{U}\mathbf{H}\mathbf{U}^T = diag\left(\nu_n\right), \quad \left(\mathbf{H}\right)_{ai,bj} = \frac{1}{2}\frac{\partial^2 E}{\partial\left(r'_a\right)_i \partial\left(r'_b\right)_j}, \tag{A6}$$

where $\mathbf{r}'_X = \mu_X^{1/2}\mathbf{r}_X$ are mass-weighted coordinates of atom X ={a, b}. We use the indexes i, j ∈ {x, y, z} to denote Cartesian coordinate components. Taking $\mathbf{U}_m$ to be the submatrix of all $U_{m,ai}$ for a given mode m, the normal-mode coordinates can then be conveniently obtained as

$$q_m = \sum_a \sum_{i=x,y,z} \left(\mathbf{U}_m\right)_{ai} \left(\mathbf{r}'_a\right)_i \tag{A7}$$

In order to convert from normal-mode to Cartesian velocities, we transform with $\boldsymbol{U}^{\mathrm{T}}$ and scale with the inverse square roots of the atomic masses:

$$\left(\dot{\mathbf{r}}_a\right)_i = \mu_a^{-1/2} \sum_m \left(\mathbf{U}_a^T\right)_{im} \cdot \left(\dot{q}\right)_m \qquad i = x,y,z \tag{A8}$$

We note that the conversion from Cartesian displacements into normal mode displacements (as needed in Appendix B) is done using the inverse transformation

$$q_m = \sum_a \mu_a^{1/2} \sum_{i=x,y,z} \left(\mathbf{U}_q\right)_{ai} \left(\mathbf{r}_a\right)_i \tag{A9}$$

APPENDIX B: DATA WEIGHTING

As described in the text, the quasiclassical trajectories can be "too classical" at low temperatures. We therefore weight all data points with the square of the quantum mechanical wave function to obtain greater weights in the quantum mechanical high probability regions. For reasons of practicality, we use the harmonic vibrational wave function,

$$\psi_v(\rho) = N_v \cdot H_v(\rho) e^{-\frac{\rho^2}{2}}, \tag{B1}$$

where ρ is a unit-less normal-mode displacement coordinate related to the normal-mode displacement coordinate by $\rho = (2\pi\nu)^{-1/2} q$ and the $H_v(\rho)$ denote the physicists' Hermite polynomials. The finite-temperature wave function is just a superposition of eigenfunctions with different levels of excitation,

$$\psi_m(\rho;\theta) = \sum_v p_v^m(\theta) \psi_v(\rho) \tag{B2}$$

where p_v^m is the appropriate Boltzmann weight for temperature θ. Finally, the total N -mode wave function is given by the product of the single-mode wave functions:

$$\Psi_{vib}(\rho_1,...\rho_N;\theta) = \prod_{m=1}^{N} \psi_m(\rho_m;\theta) \tag{B3}$$

The calculation of the total probability density for a multi-well problem would involve expanding the single-well wave functions of eq. (B3) in a global coordinate system. However, if one assumes that the vibrational probability density is separable into contributions from individual wells, the quantum weight for a certain geometry simplifies to

$$w \approx \sum_{Min} w_{Min} = \sum_{Min} \left[\Psi_{vib}^{Min}\left(\rho_1^{Min},....\rho_N^{Min};\theta\right) \right]^2, \tag{B4}$$

where the $\left\{\rho_1^{Min},....\rho_N^{Min}\right\}$ are unitless displacement coordinates w.r.t. the equilibrium structure of minimum "Min". We note that this approximation is best when tunneling through the potential

barrier is small, i.e. when the energy of the impinging particle wave is well below the barrier height and the barrier is wide. This assumption is justified for the ground-state wave function; for higher excitations the quality of the approximation deteriorates (as does the harmonic approximation). In practice we first calculate the harmonic wave function parameters for one minimum and then calculate the weights wMin along the QCT-MD trajectory. The individual weights are finally summed up to yield the total weight according to eq. (B4).

FIGURE CAPTIONS

FIG. 1: Stationary points for the cyanide-water system as calculated at the B3LYP/6-311++G** level of theory. Only the ”left” path from min1 to min2 is shown; the ”right” path is simply a mirror image. Another transition state was reported [18] connecting TS2 and TS3, but we do not include it here because it is highest in energy.

FIG. 2: Benchmark calculations: Comparison of B3LYP and MP2 relative energies to high-level CCSD(T) results. Shown basis sets are ”small Pople” (SP = 6-31+G*), ”larger Pople” (LP = 6-311++G**) as well as Dunning's aug-cc-pVnZ basis sets [22, 23].

FIG. 3: Benchmark calculations: Comparison of B3LYP and MP2 detachment energies to high-level CCSD(T) results. (a) Shown basis sets are ”small Pople” (SP = 6-31+G*), ”larger Pople” (LP = 6-311++G**) as well as Dunning's aug-cc-pVnZ basis sets [22, 23]. (b) Comparisons of VDE relative to min1 energy.

FIG. 4: Convergence of vibrational distribution.

FIG. 5: Population of the min1/min2 basins as a function of simulation time. The populations were obtained by geometry optimization along the trajectories starting in min1.

FIG. 6: CN^- photoelectron spectrum from raw vs. quantum-weighted data (QCT vs. wQCT).

FIG. 7: Monte Carlo sampling of the square of the harmonic vibrational wave function for min1 (left two columns) and min2 (right two columns) at 12 K (blue) and 300 K (red). The x-axis is in dimensionless normal-mode displacement coordinates, and Ψ^2 is plotted on the y-axis. We show here only the four modes that are lowest in energy and thus show the strongest temperature effects.

FIG. 8: Spectra obtained from QCT-MD trajectories starting in min1 and min2, respectively. Detachment energies have been weighted with the square of the (harmonic) vibrational wavefunction for min1 and min2. The 12(300)K spectra are averaged over 400(1,000) trajectories.

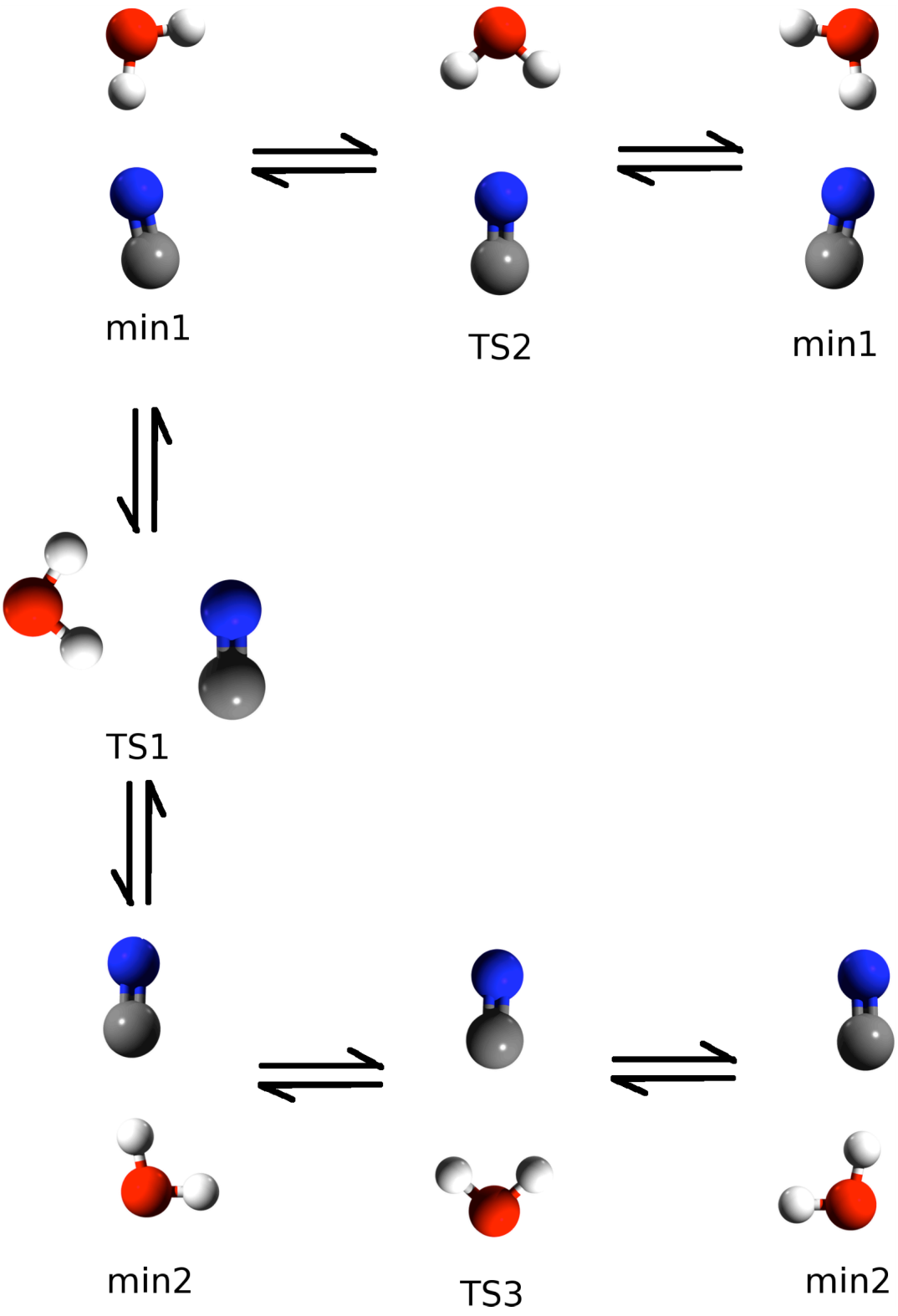

Figure 1. Lambrecht and co-workers

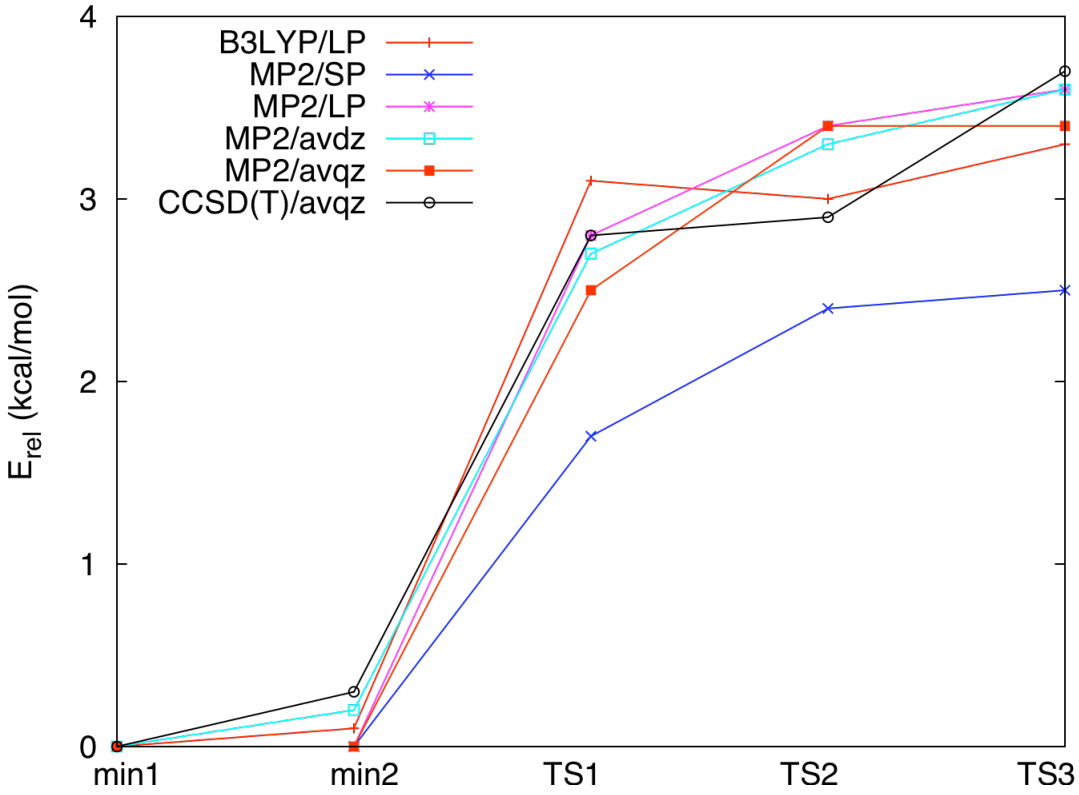

Figure 2. Lambrecht and co-workers

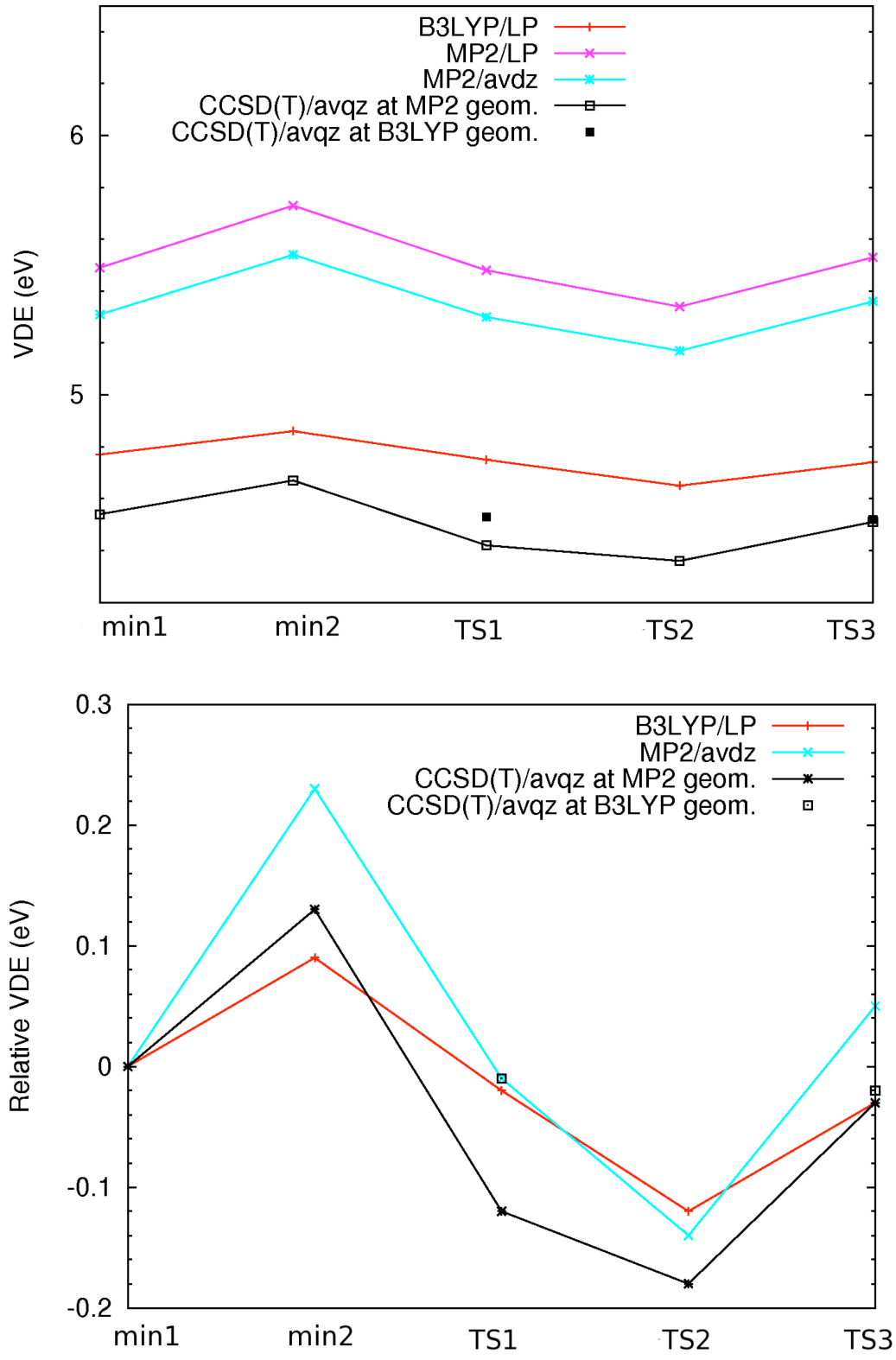

Figure 3. Lambrecht and co-workers

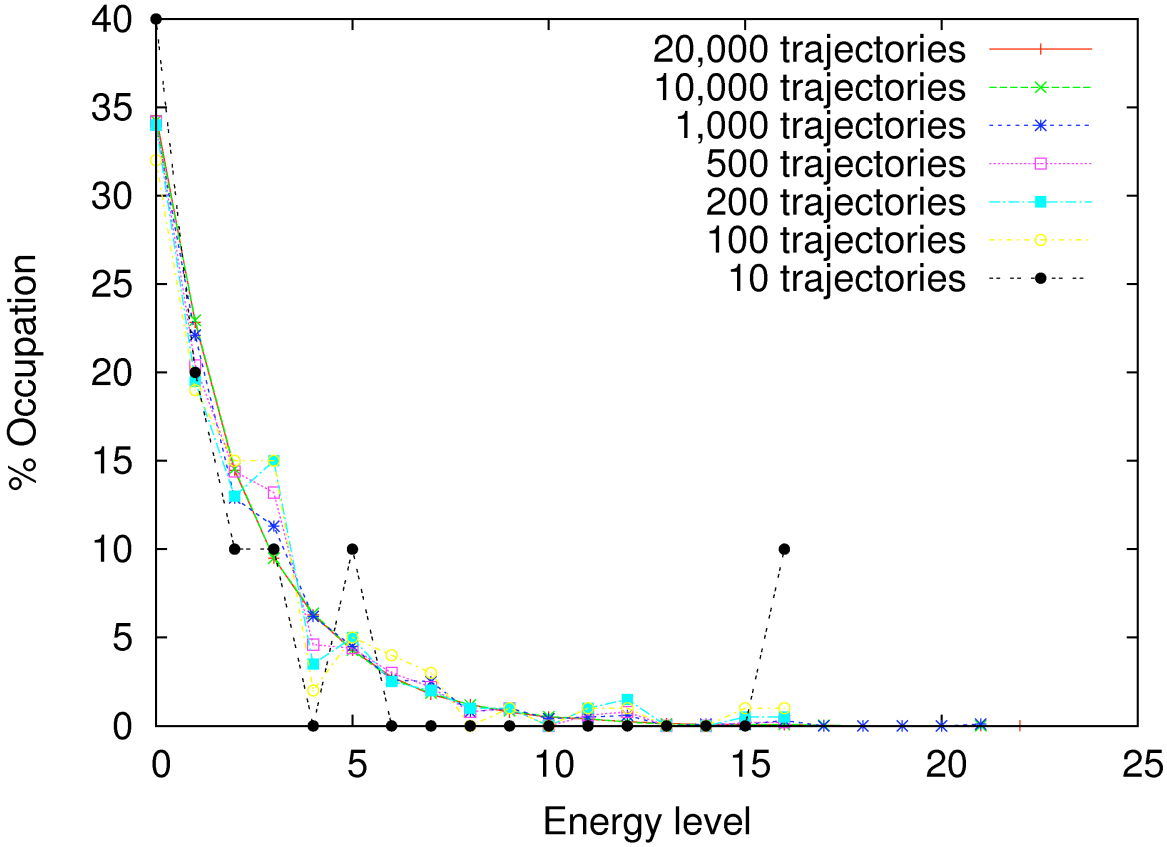

Figure 4. Lambrecht and co-workers

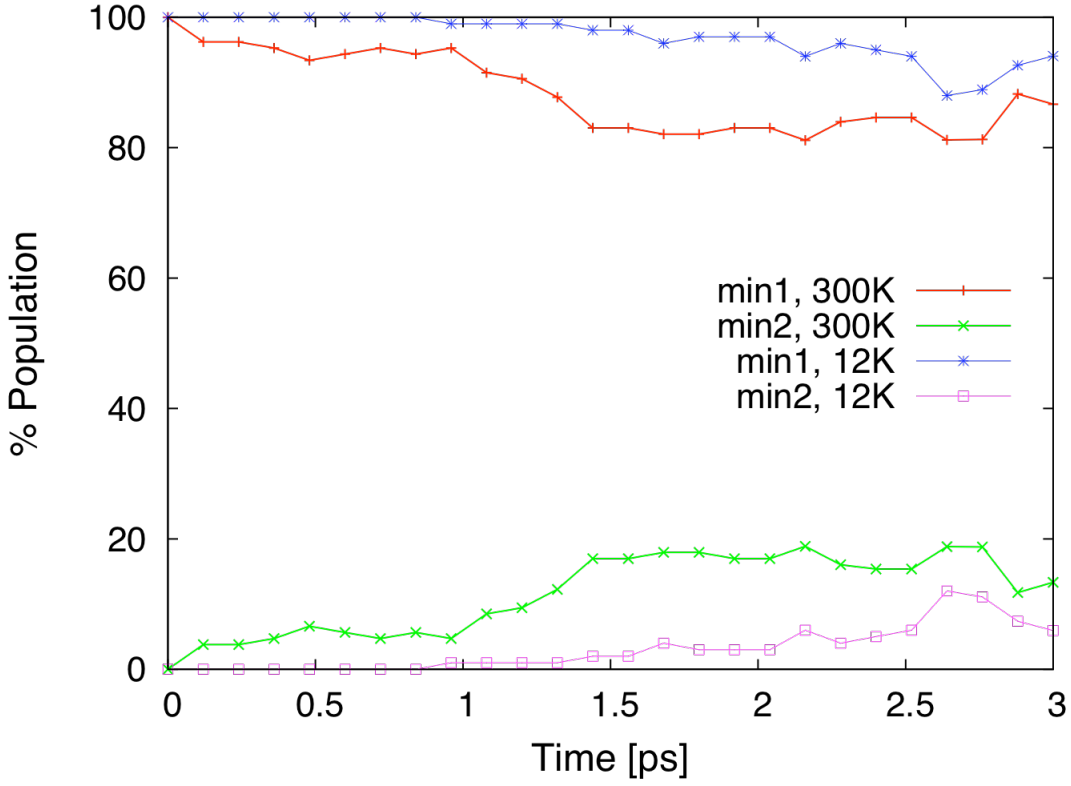

Figure 5. Lambrecht and co-workers

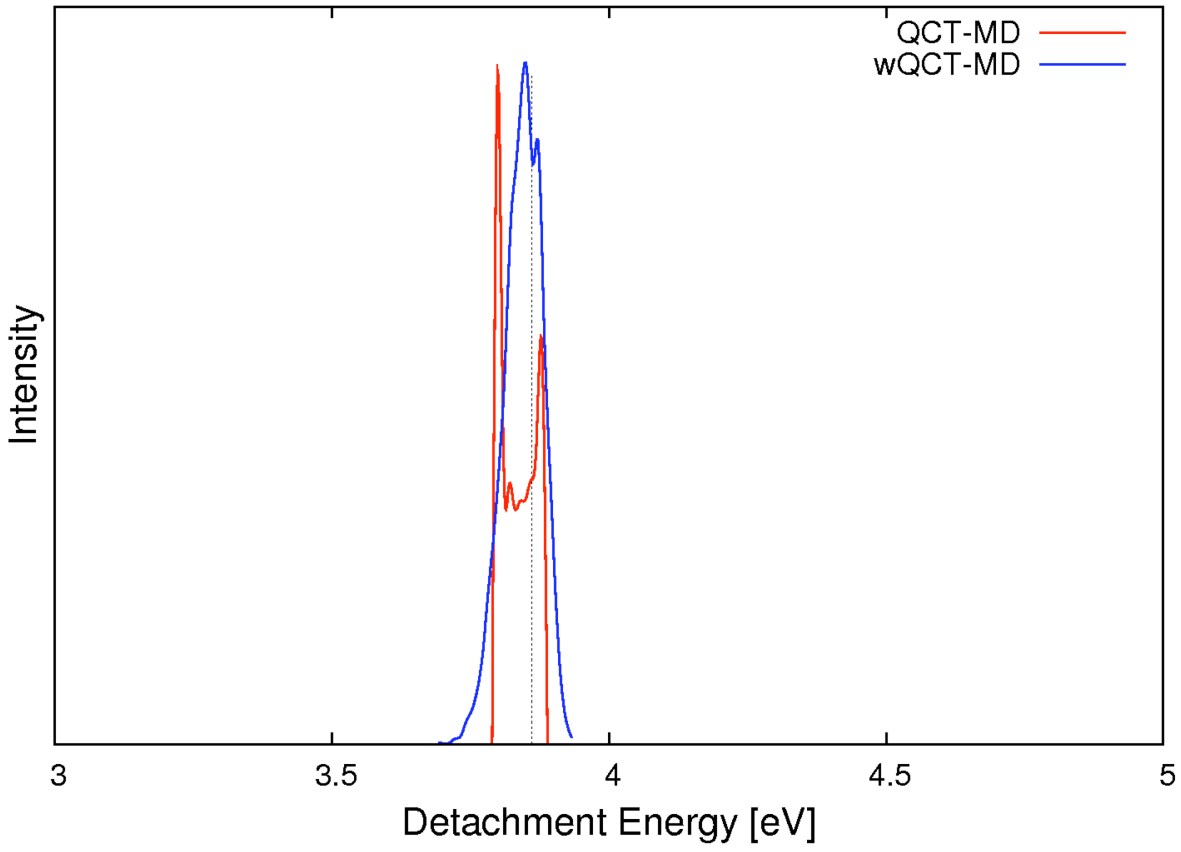

Figure 6. Lambrecht and co-workers

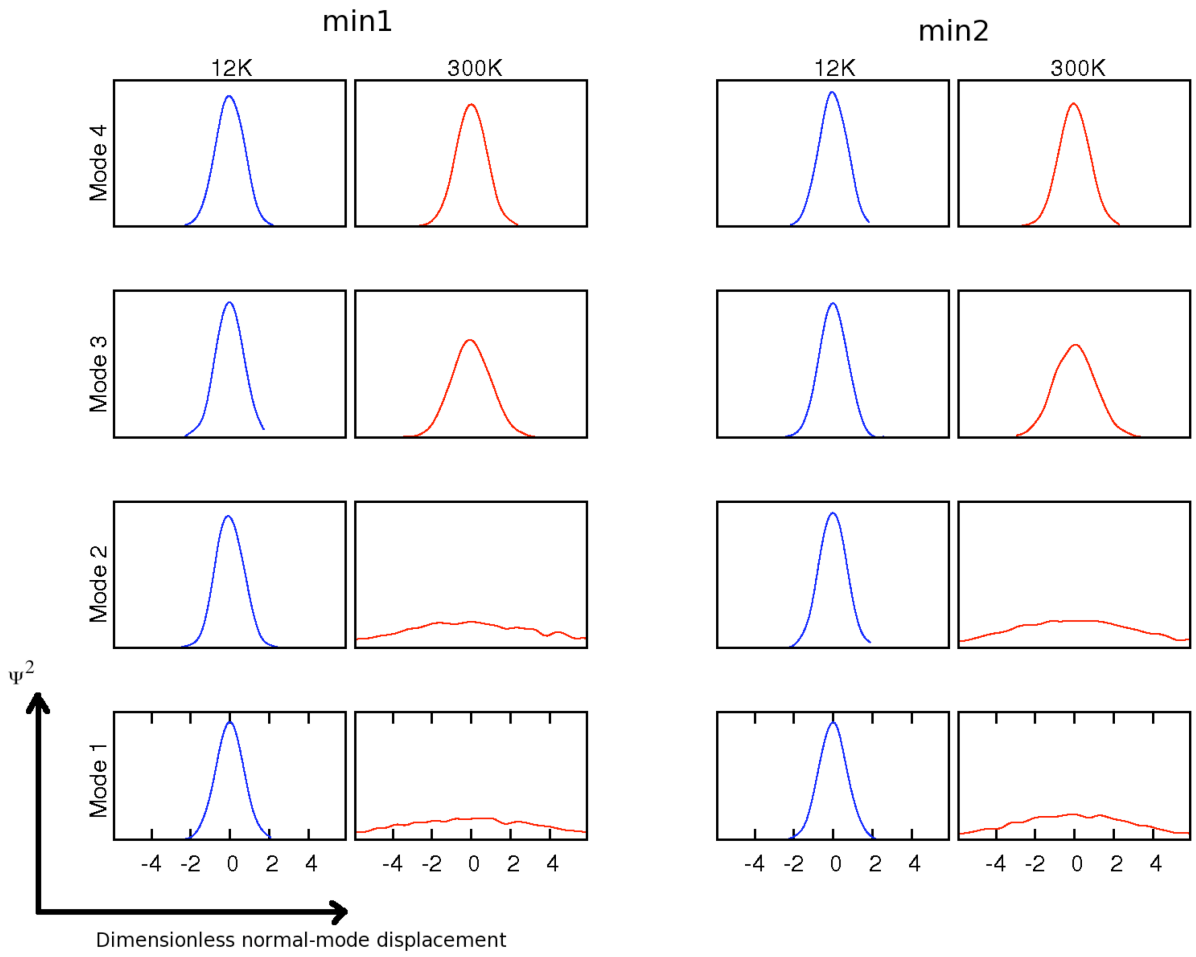

Figure 7. Lambrecht and co-workers

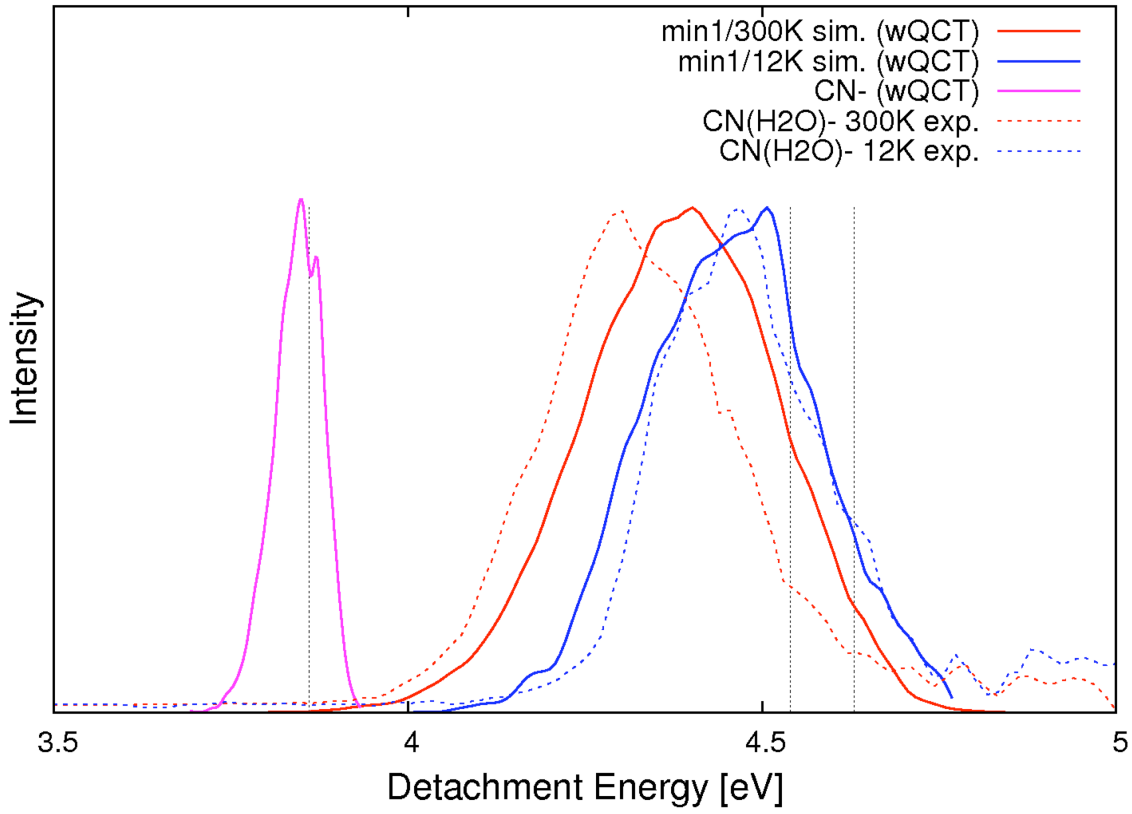

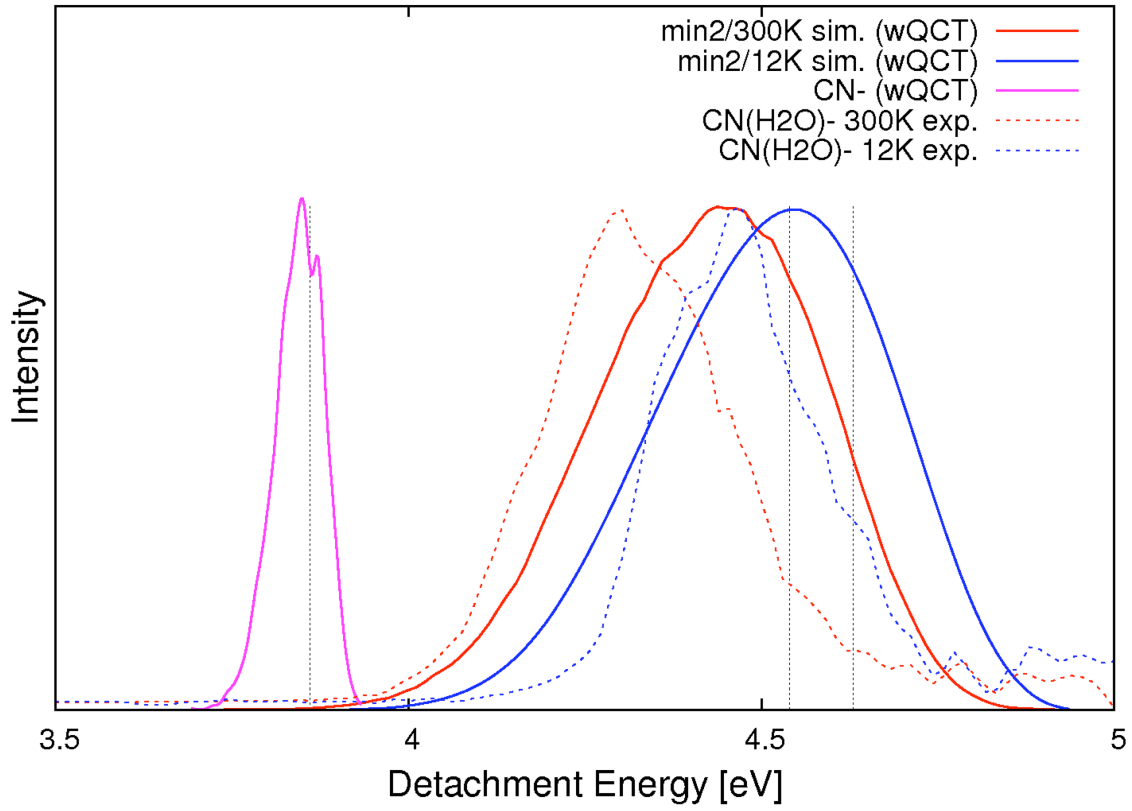

Figure 8. Lambrecht and co-workers